



A Molecular Dynamics Investigation of *Mycobacterium tuberculosis* Prenyl Synthases: Conformational Flexibility and Implications for Computer-aided Drug Discovery

Meekyum Olivia Kim^{1,*†}, Xinxin Feng^{2,†}, Ferran Feixas^{3,*†}, Wei Zhu², Steffen Lindert^{3,4}, Shannon Bogue², William Sinko³, César de Oliveira^{1,3,4}, Guodong Rao², Eric Oldfield^{2,*} and James Andrew McCammon^{1,3,4,5}

¹Department of Chemistry and Biochemistry, University of California San Diego, La Jolla, CA 92093, USA

²Department of Chemistry, University of Illinois at Urbana-Champaign, Urbana, IL 61801, USA

³Department of Pharmacology, University of California San Diego, La Jolla, CA 92093, USA

⁴Howard Hughes Medical Institute, University of California San Diego, La Jolla, CA 92093, USA

⁵Center for Theoretical Biological Physics, University of California San Diego, La Jolla, CA 92093, USA

*Corresponding authors: Meekyum Olivia Kim, mok007@ucsd.edu; Ferran Feixas, ferran.feixas@gmail.com; Eric Oldfield, eoldfie1@illinois.edu

†These authors have equally contributed to this work.

With the rise in antibiotic resistance, there is interest in discovering new drugs active against new targets. Here, we investigate the dynamic structures of three isoprenoid synthases from *Mycobacterium tuberculosis* using molecular dynamics (MD) methods with a view to discovering new drug leads. Two of the enzymes, *cis*-farnesyl diphosphate synthase (*cis*-FPPS) and *cis*-decaprenyl diphosphate synthase (*cis*-DPPS), are involved in bacterial cell wall biosynthesis, while the third, tuberculosinyl adenosine synthase (Rv3378c), is involved in virulence factor formation. The MD results for these three enzymes were then compared with previous results on undecaprenyl diphosphate synthase (UPPS) by means of active site volume fluctuation and principal component analyses. In addition, an analysis of the binding of prenyl diphosphates to *cis*-FPPS, *cis*-DPPS, and UPPS utilizing the new MD results is reported. We also screened libraries of inhibitors against *cis*-DPPS, finding ~1 μM inhibitors, and used the receiver operating characteristic–area under the curve (ROC-AUC) method to test the predictive power of X-ray and MD-derived *cis*-DPPS receptors. We found that one compound with potent *M. tuberculosis* cell growth inhibition activity was an IC₅₀ ~0.5- to 20-μM inhibitor (depending on substrate) of *cis*-DPPS, a ~660-nM inhibitor of Rv3378c as well as a 4.8-μM

inhibitor of *cis*-FPPS, opening up the possibility of multitarget inhibition involving both cell wall biosynthesis and virulence factor formation.

Key words: decaprenyl diphosphate synthase, docking, drug discovery, enzymatic mechanism, farnesyl diphosphate synthase, molecular dynamics, molecular modeling, prenyl synthase, tuberculosinyl adenosine synthase, tuberculosis

Received 6 August 2014, revised 26 September 2014 and accepted for publication 17 October 2014

With the rapid increase in resistance to antibiotics, there is a growing need for new tools, as well as new strategies, to treat bacterial infections (1,2). Antibiotics such as penicillin, methicillin, and vancomycin all target bacterial cell wall biosynthesis but have either lost or are losing their efficacy (3,4). Likewise, in tuberculosis caused by the bacterium *Mycobacterium tuberculosis*, resistance is on the rise, and new drugs active ideally against new targets are needed. One attractive approach to *M. tuberculosis* drug discovery is to inhibit isoprenoid biosynthesis enzymes involved in cell wall biosynthesis, in particular, *cis*-decaprenyl diphosphate synthase (DPPS; Rv2361c), an essential gene for the organism. DPPS converts *cis*-farnesyl diphosphate (*cis*-FPP) to *cis*-decaprenyl diphosphate (*cis*-DPP, Figure 1) in a reaction that is very similar to that catalyzed by undecaprenyl diphosphate synthase (UPPS) in non-mycobacterial systems (such as *E. coli* and *Staphylococcus aureus*), where numerous structures and inhibitors are known (5–8). *Cis*-FPP in *M. tuberculosis* is produced by *cis*-FPPS (Rv1086c) which is, however, not essential for bacterial cell growth (9). An implication of this observation is that it would be desirable to inhibit DPPS activity with both GPP as well as *cis*-FPP as substrates, as we describe here.

Cis-FPPS, *cis*-DPPS as well as UPPS are proteins that have a ζ-fold (10), as does the *M. tuberculosis* enzyme tuberculosinyl/tuberculosinyl adenosine synthase (Rv3378c) (11,12). Rv3378c is an essential enzyme in persistent, non-replicative *M. tuberculosis* that resides within macrophages. It was originally thought to be involved in formation of the putative tuberculosinol and *iso*-tuberculosinol

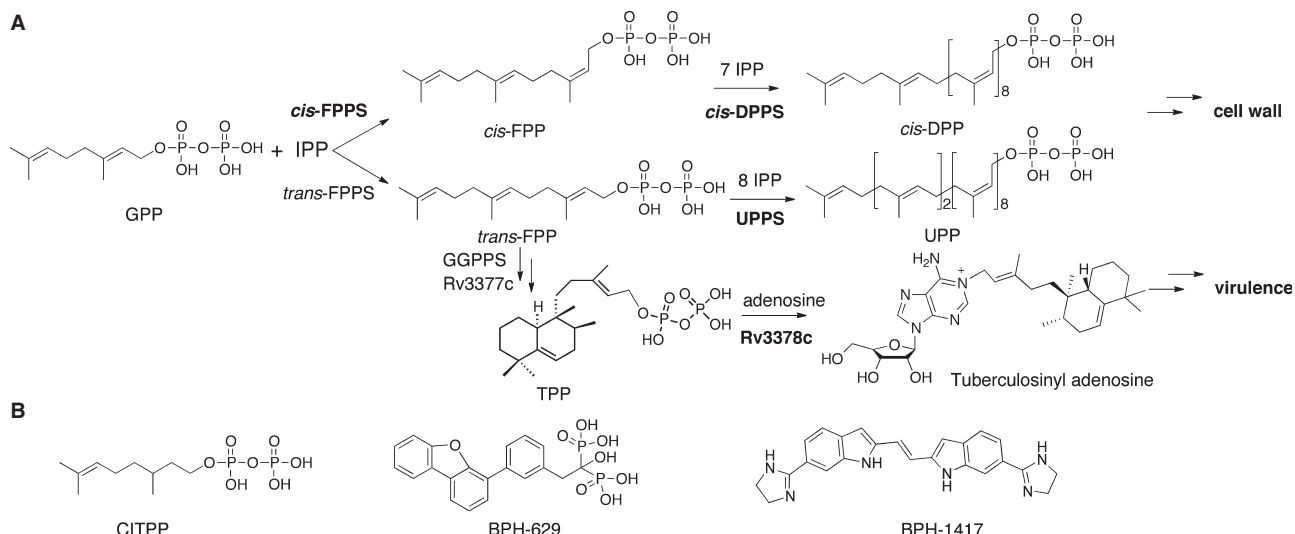


Figure 1: Reactions catalyzed by *cis*-FPPS, *cis*-DPPS, UPPS, and Rv3378c and structures of several inhibitors. (A) Reactions catalyzed. (B) The inhibitors discussed in the text.

virulence factors (13), then in formation of edaxadiene (14) and edaxadiene B (15), and most recently, tuberculosinyl adenosine (12), and inhibition of Rv3378c is likely to represent a novel anti-virulence approach to therapy (14,16). The X-ray crystallographic structures of *cis*-FPPS (17), *cis*-DPPS (17), UPPS (6) as well as Rv3378c with bound ligands are all shown in Figure 2. In UPPS, we previously found (6) that there were up to four inhibitor binding sites (sites 1–4, Figure 2C), but in *cis*-FPPS and *cis*-DPPS, there are far fewer structures and, to date, inhibitors bind only in (or close to) the active site, site 1 (Figure 2A and B). Likewise, the tuberculosinyl diphosphate substrate for Rv3378c as well as an Rv3378c bisphosphonate inhibitor binds in or near the active site, that is, site 1 in UPPS (Figure 2D) (11).

In this work, we have used molecular dynamics (MD) methods to investigate the structural plasticity of *cis*-FPPS, *cis*-DPPS, and Rv3378c and compare the results obtained with those obtained previously for UPPS (18). Specifically, we investigated the use of X-ray and MD structures to probe prenyl diphosphate chain elongation mechanisms; we screened libraries of small molecules for *cis*-DPPS inhibition activity; we used both X-ray and MD structures to see to what extent active compounds could be detected in active/decoy libraries; and finally, we investigated the idea that it might be possible to find inhibitors active against all three proteins, *cis*-FPPS, *cis*-DPPS, and Rv3378c, of interest as a route to new drug leads targeting both cell wall biosynthesis and virulence.

Methods and Materials

Molecular dynamics simulations

The following *cis*-FPPS crystal structures were used: apo *cis*-FPPS (PDB 2VFW), *cis*-FPPS in complex with

trans-FPP (PDB 2VG1), and *cis*-FPPS in complex with citronellyl diphosphate (CITPP) (PDB 2VG0) (17). *Trans*-FPP is a structural analog of the product *cis*-FPP but has two *trans* double bonds. For Rv3378c, two dimeric systems based on two different crystal structures were prepared for the MD simulations: apo state (PDB 3WQL) and the inhibitor BPH-629 bound system (PDB 3WQM) (11). For each system, tleap program in Amber 11 was used to neutralize the systems by adding Na⁺ counterions and solvating using a TIP3P water box (19,20). Minimization using the Sander module of Amber 11 was carried out in two stages: 1000 steps of minimization of the solvent and ions with the protein and ligand restrained with a force constant of 500 kcal/mol/Å², followed by a 2500-step minimization of the entire system (21,22). An initial 20-ps MD simulation with a restraint of 10 kcal/mol/Å² on the protein and ligand was then performed to heat the system to 300 K. Subsequently, 500-ns MD simulations were carried out on each system under the NPT ensemble at 300 K using Amber 11 with the ff99SBildn force field (21–23). Periodic boundary conditions were used, along with a non-bonded interaction cutoff of 10 Å for particle mesh Ewald (PME) long-range electrostatic interaction calculations. Bonds involving hydrogen atoms were constrained using the SHAKE algorithm, allowing for a time step of 2 fs (24).

For DPPS, we used the following structures: apo DPPS (PDB 2VG4), DPPS in complex with IPP bound to monomer B (PDB 2VG2), and DPPS in complex with CITPP bound to both monomers (PDB 2VG3) (17). Glycerol, phosphate, chloride, and sulfate ions used in crystallization were removed from the crystal structures while keeping the magnesium ions, which are essential for catalysis (25). The protonation states of ionizable amino acid residues were determined using PROPKA and H++ (26–33). Ligands were optimized using the B3LYP functional and a

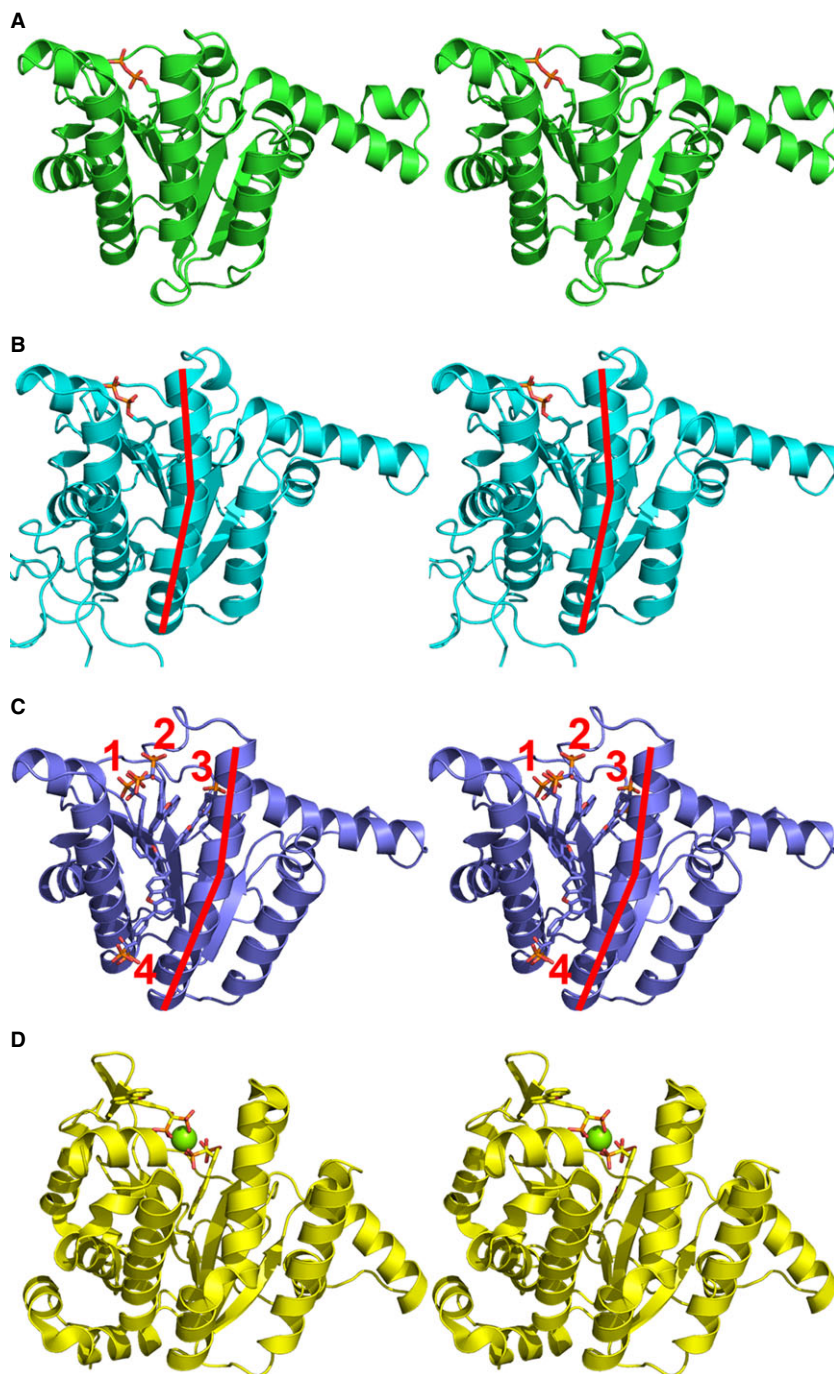


Figure 2: X-ray crystallographic structures of interest, shown as stereo views. (A) *M. tuberculosis* *cis*-FPPS (Rv1086c; PDB ID 2VG0) + CITPP. (B) *Cis*-DPPS (Rv2361c; PDB ID 2VG3) + CITPP. (C) *E. coli* UPPS (PDB ID 2E98) + BPH-629. The numbers 1, 2, 3, and 4 denote the four ligand binding sites found in UPPS. (D) Rv3378c (PDB ID 3WQM) + BPH-629. The Mg^{2+} ion coordinating the ligand and protein is shown as a green sphere. The red lines indicate where the $\alpha 3$ helix can bend in *cis*-DPPS and UPPS; this helix is 'broken' in Rv3378c.

6-31G(d) basis set in Gaussian 03 and parameterized using Antechamber and RESP in Amber Tools 11 with the General AMBER force field (GAFF) (21,34–36). Proteins were solvated with TIP3P water molecules with a buffer region of 10 Å in all directions and neutralized with counterions using the tleap program (19,20). Each DPPS system was equilibrated using *sander* with the MPI module of Amber 11 and the ff99SBildn force field (21–23). Water molecules were minimized with periodic boundary conditions in a constant volume with the protein and ligands fixed with a force constant of 2.0 kcal/mol/Å², followed by

a 150 ps MD simulation in the NPT ensemble. The entire system was minimized and heated from 0 to 300 K over 500 ps, followed by two 20-ps MD simulations in the NVT and NPT ensembles, respectively. Five 500-ns MD simulations were performed on each DPPS system in the NVT ensemble with a Langevin thermostat using the PMEMD module of Amber 11 with the ff99SBildn force field using a graphics card (21–23). The PME summation method was used to describe the long-range electrostatic interactions, and short-range non-bonded interactions were truncated at 8 Å in the periodic boundary conditions.



Volume calculations

Active site volumes were calculated using the POVME program with frames extracted every 25 ps from the simulations (37). Points describing the binding pocket were manually defined along the hydrophobic cavity of monomer B of the apo DPPS structure by locating a sphere with a 1 Å diameter at each point, removing any points where van der Waals clashes occurred with the protein. All points defined for monomer B of apo DPPS were used for *cis*-FPPS as well by aligning the trajectories to monomer B of apo DPPS. Monomer A was also aligned to monomer B so that the results were comparable with the same points defining the active pocket. All ligands simulated in the MD were removed prior to volume calculation. The same procedure was repeated for Rv3378c and the UPPS X-ray crystallographic structures.

Principal component analysis

To compare the results obtained here with previous PCA results on UPPS obtained from 21 X-ray crystallographic structures (7), the X-ray crystal structures of *cis*-FPPS and DPPS that were used in the MD simulations were projected onto the UPPS PC space. Subsequently, the trajectories of the apo states of *cis*-FPPS and DPPS were projected onto the UPPS PC space, using the Bio3D package (38).

Ligand docking

We docked a series of prenyl diphosphates with various chain lengths to *cis*-FPPS, *cis*-DPPS, and UPPS using the X-ray crystallographic structures 2VFW, 2VG4, and 2E98, respectively, in addition to the most open conformations taken from the MD simulations. The receptors were prepared by setting the receptor docking grid center to C1 of the cocrystallized ligand (CITPP) in the 2VG3 structure. Self-docking of the ligand CITPP was carried out as a preliminary test of the ability of the receptor grid center to recover the crystallographic pose of the ligand. The size of the inner and outer grid boxes was set to 14 Å and 20 Å in each direction, respectively. The prenyl diphosphates were then generated with various lengths (from C₁₀ to C₆₀) with Maestro in Schrödinger Suite 2012^a. The molecules were further prepared using LigPrep with the OPLS2005 force field using all possible tautomers and stereoisomers generated in the pH range 5.2 ± 9.2, using Epik^{b,c} (39,40). Docking was carried out using Glide XP precision with Glide 5.8^d (41–43).

In vitro screening for *cis*-DPPS, *cis*-FPPS, and Rv3378c inhibitors

We screened an in-house library of 19 compounds against DPPS using *cis*-FPP as substrate, 43 compounds using GPP as substrate and 53 compounds using *trans*-FPP as substrate. The structures and IC₅₀ values for the active compounds (IC₅₀ values in the range 31 nM to 880 μM) are

shown in Figures S1–S3. DPPS was expressed and purified as described previously (11), as were the DPPS inhibition assays (18). Briefly, the condensation of IPP and GPP, FPP, or *cis*-FPP catalyzed by DPPS was monitored using a continuous spectrophotometric assay for diphosphate release (44) in 96-well plates with 200 μL reaction mixtures containing 400 μM 2-amino-6-mercapto-7-methylpurine (MESG), 25 μM GPP, *cis*-FPP or *trans*-FPP, 200 μM IPP, 25 mM Tris–HCl (pH 7.5), 0.01% Triton-X-100, and 1 mM MgCl₂. The IC₅₀ values were obtained by fitting the inhibition data to a rectangular hyperbolic dose–response function in OriginPro 8.5 (OriginLab, Northampton, MA, USA). The IC₅₀ values for the most active hits were verified by radiometric assay as follows. A mixture of 15 μM *cis*-FPP, 100 nM DPPS, and inhibitors in the assay buffer (25 mM Tris–HCl, 1 mM MgCl₂, 0.01% Triton-X-100) was incubated for 10 min at 25 °C. 1.8 μL of 25 μM IPP (1% 1-³H IPP, 15 μCi/mL, American Radiolabeled Chemicals, Inc.) was then added. The reaction was incubated at 37 °C for 10 min before quenching with 500 μL saturated NaCl solution. The saline solution was extracted with 500 μL butanol by vortexing, and 300 μL of the organic layer was transferred into scintillation vial for radiation readout. IC₅₀ values were fitted in Origin 9.0 by analyzing the dose–response curves. For *cis*-FPPS, protein expression, purification, and inhibition were all carried out as reported previously (17).

For Rv3378c, protein expression and purification were all carried out as reported previously (11). For inhibition assay of Rv3378c, a mixture of 100 μM TPP, 100 μM adenosine, 75 μg/mL Rv3378c, and inhibitors in the assay buffer (25 mM Tris–HCl, 1 mM MgCl₂, 0.01% Triton-X-100) was incubated for 2 h at 37 °C. Tuberculosinyl adenosine formation was determined by LC/MS carried out using an Agilent LC/MSD Trap XCT Plus instrument. Compounds were separated on a Gemini 3 μm C18 110 Å (100*2 mm) column from Phenomenex using a 0–100% methanol (in water with 0.1% formic acid) gradient and monitored using positive-ion mode ESI at m/e = 540.4.

Virtual screening

To incorporate receptor flexibility into computer-aided drug discovery as an application of the relaxed complex scheme, we carried out a virtual screening (VS) of the known actives (Figures S1–S3) against an ensemble of 30 different DPPS conformations (45). The receptor structures were selected by clustering the apo DPPS trajectory based on the active site volumes. Any potential ligand binding sites in DPPS were first explored using the computational solvent mapping program FTMap, which suggests druggable hot spots in a protein by docking a number of small organic fragments into the protein (46). Upon evaluating the results of FTMap (see Results and Discussion), we set the receptor grid center as the native binding pocket of the enzyme and used the same protocol as described above for ligand docking for receptor preparation.

The compound libraries consisted of the 43 (GPP substrate), 19 (*cis*-FPP), or 53 (*trans*-FPP substrate) experimentally tested active inhibitors with IC_{50} s between 0.03 and 20 μ M (GPP substrate), 0.6 μ M and 90 mM (*cis*-FPPS substrate), or 0.65 μ M and 880 mM (*trans*-FPP substrate), together with 1000 decoys of average molecular weight 400 Da, from the Glide Decoy Set. The ligands were prepared using LigPrep in Schrödinger Suite 2012 with the OPLS2005 force field, and tautomers and stereoisomers were generated within the pH range of 5.2 ± 9.2 using Epik^{b,c} (39,40). The VS was carried out with Glide standard precision (SP) using Glide 5.8 d (41–43). The VS results were analyzed using the receiver operating characteristic (ROC) and the area under the curve (AUC) metrics. ROC is a widely used method to evaluate the performance of VS in distinguishing known actives from decoy compounds (47). The AUC then quantitatively compares the performance of different receptors; values of 0.5 correspond to a random selection of a compound in the library.

Results and Discussion

Structural flexibility of *cis*-FPPS, *cis*-DPPS, and UPPS

To explore the conformational flexibility of the active sites of *cis*-FPPS and *cis*-DPPS, fluctuations in the volume of the binding pocket during the MD simulations were analyzed for each monomer in the various systems. We begin by considering *cis*-DPPS, as this is thought to be a key new drug target, while *cis*-FPPS appears to be non-essential (9).

We show in Figure 3A–C the binding pocket volume fluctuations during the MD simulations for each monomer of the DPPS systems investigated: apo (Figure 3A), IPP (Figure 3B), and CITPP bound structures (Figure 3C). There are several clear transitions between open and closed states in the active site, indicating the large structural flexibility of the binding pocket. This flexibility is most pronounced in the apo and IPP *cis*-DPPS simulations (Figure 3A and B). An opening of the active site of apo *cis*-DPPS is particularly noticeable, as shown in detail in Figure 4, in which the pocket opens up from 455 \AA^3 in the X-ray crystal structure (Figure 4A) to 882 \AA^3 in the early stage of the simulation (Figure 4B). Additional transitions between open and closed states of the active site in the ~ 200 \AA^3 and 700 \AA^3 range are subsequently observed, the large range in volumes seen clearly indicating the flexible nature of the active site, the largest volumes likely being related to the need to house the large (C_{50}) *cis*-DPP product. Interestingly, the presence of the (C_{10}) substrate-like ligand (CITPP, Figure 1B), a structural analog of GPP, restricts the active site volume to ~ 400 \AA^3 during the entire simulation (Figure 3C), due presumably to strong hydrogen bonding networks and salt bridges between the diphosphate moiety of CITPP and Arg residues, together with hydrophobic interactions in the active site.

Figure 4 clearly shows the large volume differences observed between the closed (X-ray) and most open (MD) structures. This arises from a pronounced bend in helix $\alpha 3$ (between residues S126 and F136), which is very similar to what was previously seen in UPPS (48). This bent helix is present in both the apo *cis*-DPPS X-ray structure and the CITPP X-ray structure (Figure 2B) and corresponds to a small pocket volume. However, as discussed below in more detail, this pocket is too small to accommodate the *cis*-DPP product, which can, however, be docked to the most open MD structure (Figure 4B), and this bend motion is likely to be important in catalysis. Interestingly, we observe a closing of the large pocket during an MD simulation in which we docked CITPP to an open structure (Figure 5). In this simulation, the initial structure had a volume of 756 \AA^3 (Figure 5B), but this rapidly decreased during the simulation as the pocket closed (Figure 5B and C) with the closed structure having a volume $V \sim 230$ \AA^3 . Thus, the substrate-like ligand induces formation of a closed state. Similar effects are also seen with substrate-like ligands in UPPS, as described in more detail below, and are important in the context of virtual screening and in catalysis.

Cis-FPPS, producing the C_{15} isoprenoid *cis*-FPP, has not unexpectedly a smaller active site than does *cis*-DPPS, which synthesizes the C_{50} compound, DPP. The active site of *cis*-FPPS during the MD simulations also remains in a relatively closed state, fluctuating only up to $V \sim 480$ \AA^3 , even in the absence of any ligands (Figure 3D). In the presence of the small, substrate-like inhibitor CITPP in both monomers, the active site volume ($V \sim 300$ \AA^3) remains quite constant along the entire trajectory (Figure 3E). CITPP is a known inhibitor of *cis*-FPPS, and as with CITPP binding to *cis*-DPPS (Figures 3C and 5C), CITPP stabilizes the closed conformation. With the non-native substrate all-*trans*-FPP, the active site volume is larger (Figure 3F), but again does not approach the much larger volumes seen in apo *cis*-DPPS.

These results are all of interest in the context of chain length regulation during catalysis, as discussed in more detail in the following sections, as well as in inhibitor discovery.

Pocket volume and principal component analysis of *cis*-FPPS, DPPS, and UPPS

We next sought to compare the structures of *cis*-FPPS, *cis*-DPPS, and UPPS in detail using pocket volume and principal component analyses. Pocket volume results are shown in Table 1 for all three proteins (as well as for Rv3378c), using both X-ray and in some cases, MD results.

For *cis*-FPPS, the pocket volumes seen in X-ray crystallographic structures are all in the range 240–327 \AA^3 , and for *cis*-DPPS, 227–461 \AA^3 . These volumes are small and are

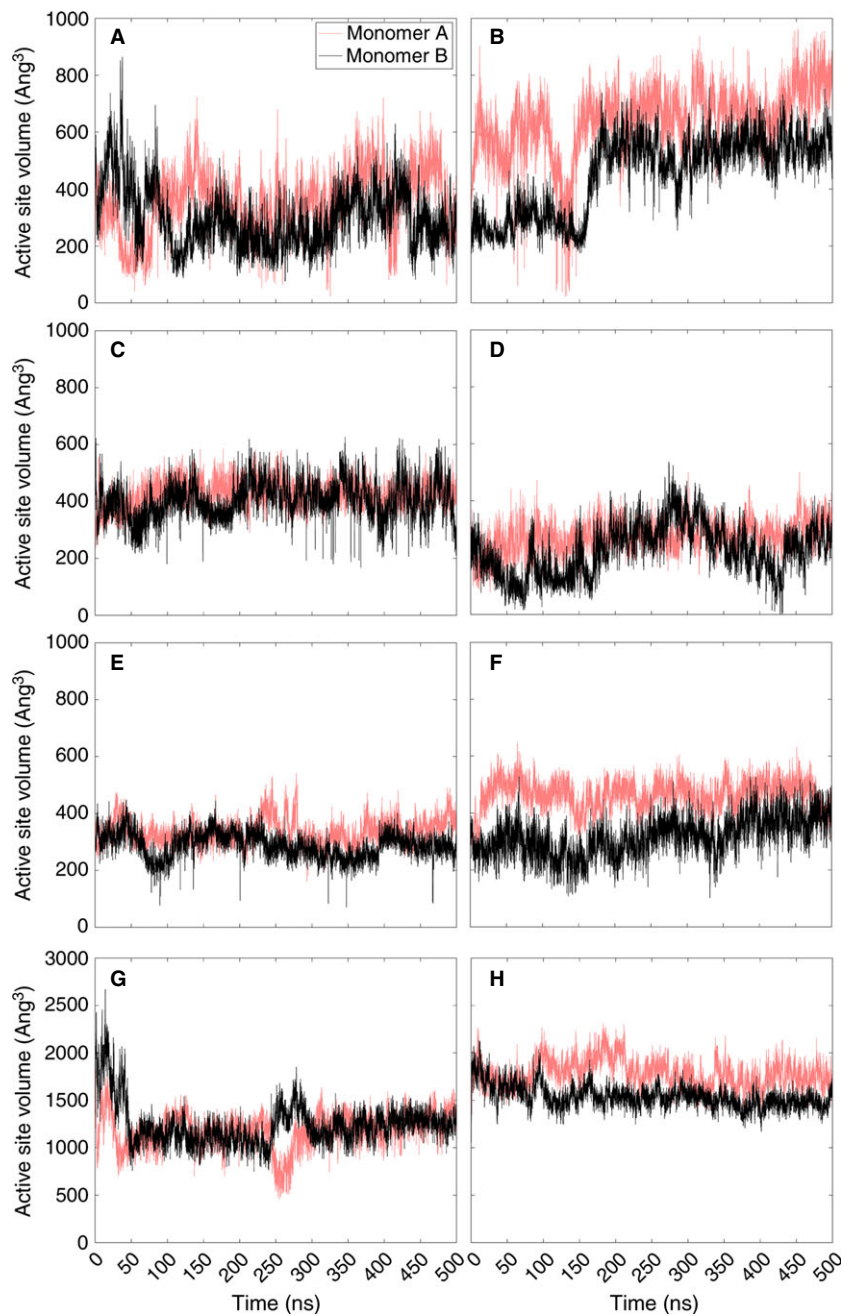


Figure 3: Volume fluctuations of the active site in each monomer of the various *cis*-FPPS, DPPS, and Rv3378c systems. (A) Apo DPPS. (B) DPPS + IPP. (C) DPPS + CITPP. (D) Apo *cis*-FPPS. (E) *Cis*-FPPS + CITPP. (F) *Cis*-FPPS + *E,E*-FPP. (G) Apo Rv3378c. (H) Rv3378c + BPH-629. Red and black lines are for monomers A and B, respectively.

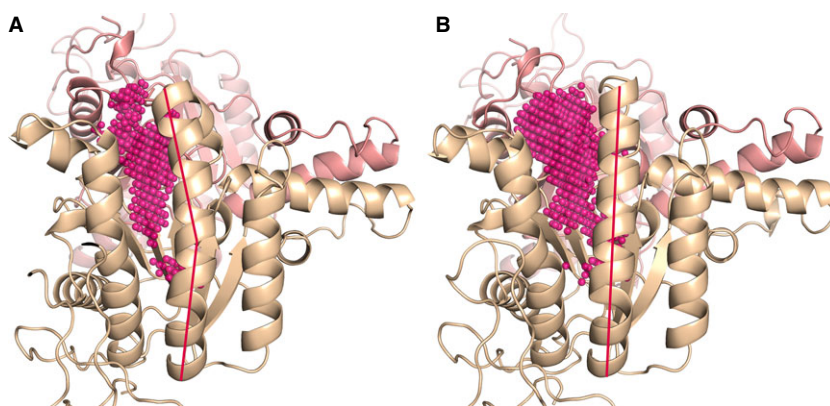


Figure 4: Comparison of the active site volumes. (A) Apo *cis*-DPPS in the X-ray crystal structure with $V = 455 \text{ \AA}^3$. (B) The most open state in the MD simulation with $V = 882 \text{ \AA}^3$.

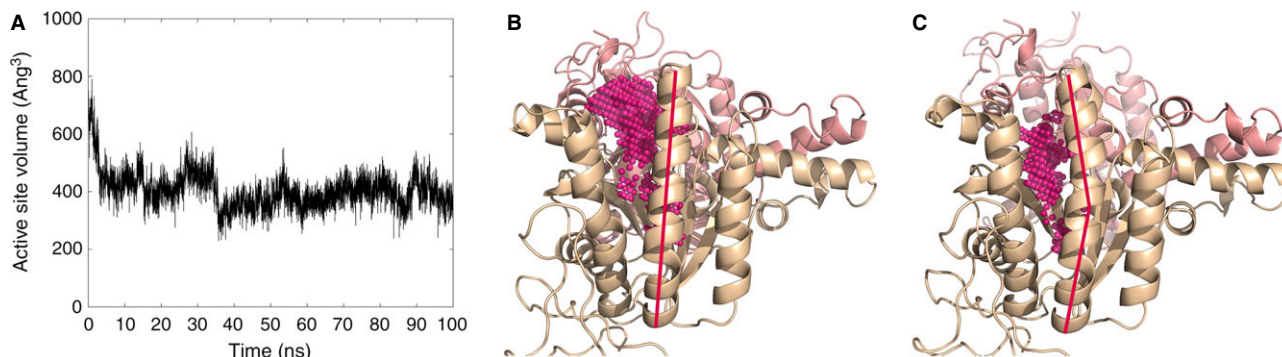


Figure 5: (A) Rapid closure of the expanded active site of monomer B in *cis*-DPPS upon incorporation of CITPP. (B) Binding pocket of the apo starting structure ($V = 756 \text{ \AA}^3$). (C) Pocket in the closed state of the active site after MD in the presence of CITPP ($V = 229 \text{ \AA}^3$). The helix bend illustrated helps close the pocket.

similar to these found in substrate-like liganded UPPS structures ($270\text{--}315 \text{ \AA}^3$, Table 1). In the most open MD structures, the volumes in *cis*-FPPS and *cis*-DPPS increase to 537 \AA^3 and to 882 \AA^3 , respectively. These values are more similar to those found in the ‘ajar’ and open UPPS structures (range $456\text{--}1440 \text{ \AA}^3$) but are clearly, on average, smaller—most likely due to the fact that the UPPS structures in many cases have multiple bound ligands (up to 4), while *cis*-FPPS and *cis*-DPPS do not. However, it is possible that site 4 in UPPS is not actually involved in catalysis, although it can house potent inhibitors.

An attractive method for structure comparison is to use a principal component analysis (PCA) method as in PCA, there are more parameters to be compared. In previous work on UPPS (7), we found that there were three UPPS clusters in (PC1, PC2) principal component space: closed (substrate-like) structures, ‘ajar’ (apo and other non-bisphosphonate inhibitor) structures, and open (bisphosphonate inhibitors—often with multiple ligands) structures. As can be seen in Figure 6A, there are 3 main regions in PC space for *cis*-FPPS, *cis*-DPPS, and UPPS: A, B, and C, respectively, where the UPPS structures are circled. The B and C clusters (‘ajar’ and open, respectively) are solely populated by UPPS structures, while the A cluster contains the closed UPPS structures in the circle as well as all of the *cis*-FPPS and *cis*-DPPS X-ray structures.

As noted above, the pocket volumes seen (Table 1) in the X-ray structures of *cis*-DPPS are too small to accommodate a *cis*-DPP ligand ($V = 879 \text{ \AA}^3$), and we were unable to dock *cis*-DPP to any of the *cis*-DPPS structures, although we could dock them to the MD structures. We thus next investigate the MD results in more detail. A PCA analysis of the *cis*-FPPS and *cis*-DPPS MD trajectories is shown in Figure 6B (*cis*-FPPS, green dots; *cis*-DPPS, yellow dots) and clearly shows that a large conformational space is sampled in the simulations—although interestingly the spaces sampled do not quite overlap the UPPS B and C domains, due presumably at least in part to the fact that the UPP is slightly larger than DPP.

With Rv3378c, the pocket volumes for essentially all X-ray structures have $V \sim 1000 \text{ \AA}^3$ (Table S1), and the pockets remain quite open, with or without a bound inhibitor (Figure 3G and H). As Rv3378c is not a *cis*-prenyl synthase but rather a tuberculosinyl adenosine transferase (that happens to have a similar ζ -fold structure), it appears that a larger pocket may be required here because both substrates are relatively large but additional X-ray structures are needed to probe the Rv3378c mechanism of action in detail.

Chain elongation mechanisms of *cis*-FPPS, *cis*-DPPS, and UPPS

The active site volume and PC analysis results described above indicate that the *cis*-FPPS and *cis*-DPPS X-ray structures correspond to the closed state of UPPS in which case, certainly with *cis*-DPPS, it would be impossible to dock in a C_{50} product, as we indeed found experimentally (data not shown). We thus next used the Glide program to dock prenyl diphosphates containing from 2 to 12 prenyl groups (i.e., $C_{10}\text{--}C_{55}$) to *cis*-FPPS, *cis*-DPPS as well as UPPS using the most open (largest volume) MD-based protein structures. Docking poses for the corresponding products are shown in Figure 7A–C, and docking scores as a function of the prenyl chain length (FPP = C_{15} ; DPP = C_{50} , etc.) are shown in Figure 7D. This approach is similar in spirit to that used by Wallrapp *et al.* (49) to study docking to trans-prenyl transferases, but here we use MD structures to account for the protein conformational flexibility.

For UPPS (green dots, Figure 7D), we see an expected ‘U-shaped’ curve in which the best docking score is found with a C_{50} species. The binding energy/docking score becomes slightly worse with an increase in chain length, and C_{60} could not be docked. For *cis*-DPPS, the minimum energy is at C_{30} with C_{35} slightly higher and C_{50} much higher (Figure 7D), while C_{55} and C_{60} could not be docked. The results with *cis*-FPPS show strongest binding with C_{10} , with C_{15} and C_{20} both being $\sim 2\text{--}3 \text{ kcal/mol}$

Table 1: Computed active site volumes and PC values and corresponding conformational states for *cis*-FPPS, *cis*-DPPS, UPPS, and Rv3378c

System	PDB ID	Pocket Volume (Å ³)	Ligand Volume (Å ³)	PC1	PC2	Conformation and average pocket volume (Å ³)	
<i>Cis</i> -FPPS	2VFW	240	0	-10.77	-2.42	Closed	
	2VG0	241	272	-11.14	-1.48	269 ± 50	
	2VG1	327	344	-10.26	-2.42		
	2VFW Open state	537	0	-	-	Open (MD) 537	
<i>Cis</i> -DPPS	2VG2	227	189	-9.53	2.03	Closed	
	2VG4	455	0	-9.24	1.77	381 ± 133	
	2VG3	461	272	-8.94	1.63		
	2VG4 Open state	882	0	-4.62	1.29	Open (MD) 882	
UPPS	SaUPPS	155	344	-10.87	4.2	Closed (substrate bound)	
	1X07	270	189	-10.81	-1.16	272 ± 68	
	1X09	307	189	-12.58	1.28		
	1X06	312	353	-9.75	-1.41		
	1X08	315	353	-10.58	-1.13		
	3SGV	456	351	0.99	-0.55	Ajar (apo/non-bisphosphonate bound)	
	4H2M	581	397	1.71	1.69	726 ± 167	
	4H2J	672	430	1.97	2.08		
	3TH8	765	338	0.61	4.01		
	4H38	804	387	1.87	1.70		
	4H3C	870	342	2.60	1.60		
	3SH0	932	329	4.57	2.29		
	2E9A	948	357	2.34	-3.90	Open (bisphosphonate bound)	
	2E99	987	366	4.04	-4.80	982 ± 31	
	2E9D	1010	357	3.22	-3.15		
	4H3A	1048	309	2.52	1.49	Ajar (apo/non-bisphosphonate bound)	
	4H2O	1079	414	1.73	2.50	1064	
	2E98	1082	355	5.45	-6.09	Open (bisphosphonate bound) 1082 ± 22	
		3QAS	1169	0	1.00	1.72	Ajar (apo/non-bisphosphonate bound)
		3SGX	1213	393	4.19	6.11	1205 ± 32
	3SGT	1232	327	2.03	-0.13		
	2E9C	1440	445	2.90	-4.18	Open (bisphosphonate bound) 1440	
Rv3378c	4CMX	131	246			Closed 131	
	3WQK	714	0			Open	
	3WQM	808	355			1046 ± 256	
	4KT8	905	412				
	3WQN	1051	412				
	4CMV	1171	152				
	3WQL	1240	0				
	4CMW	1436	152				

higher energy and C₂₅ higher still. Longer chain species again failed to dock. With *cis*-DPPS and UPPS, it can be seen that there is no energy minimum at the normal product chain length (C₅₀ or C₅₅). Rather, with DPPS, the binding energy (Glide score) for C₅₀ (in DPPS) is ~4 kcal/mol higher than with C₃₀, while C₅₅ did not dock. Likewise, with UPPS, the minimum is at C₅₀ with the C₅₅ product ~1.5 kcal/mol higher, and C₆₀ did not dock. Clearly, these results indicate that once the chain becomes sufficiently long, its binding energy increases, which results in product being released from the protein. The product ('P') chain lengths are indicated in Figure 7D. With *cis*-FPPS, the binding energy of the product (C₁₅) is again ~3 kcal/mol higher than with C₁₀ and is about the same as observed

with the C₂₀ species (~-5 kcal/mol), C₂₅ is a weaker binder, and all longer chain species (C₃₀ through C₆₀) failed to dock. So, the docking results all indicate that there are significant decreases in the binding energy of products (versus shorter reaction intermediates).

DPPS inhibition and receptor flexibility

We next sought to see to what extent we could use the MD structures in computational docking/virtual screening. As noted above, DPPS (Rv2361c) is an essential gene in *M. tuberculosis* and converts *cis*-FPP to *cis*-DPP (Figure 1A). *Cis*-FPPS is, however, not an essential gene, which suggests that GPP (the *cis*-FPPS substrate) can still

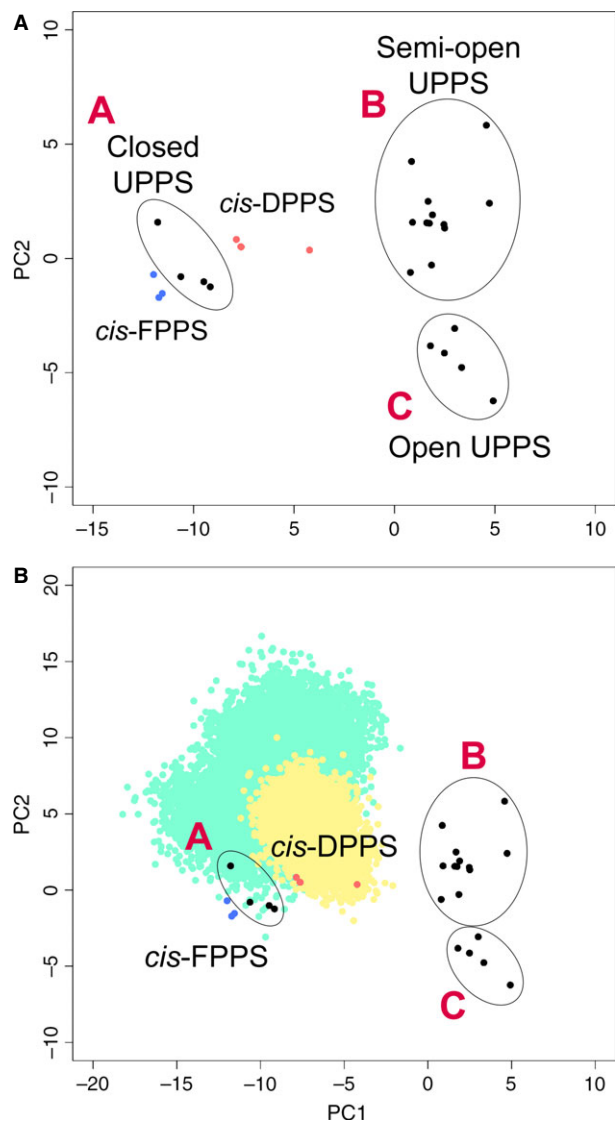


Figure 6: Separation of conformational states for different enzymes revealed by principal component analysis. (A) Projection of X-ray crystallographic structures of *cis*-FPPS (blue) and DPPS (red) onto UPPS PC space. Distinctive conformational states corresponding to UPPS structures are marked. (B) Projection of trajectories of *cis*-FPPS (green) and DPPS (yellow) onto UPPS PC space.

be converted to long chain prenyl diphosphates (by *cis*-DPPS), which can then be used in cell wall biosynthesis. Ideally, then, an inhibitor should inhibit *cis*-DPPS with either GPP or *cis*-FPP as substrate. We thus next screened our in-house library of putative prenyl synthase inhibitors against *cis*-DPPS using GPP, *cis*-FPP, and *trans*-FPP (which can also make long chain prenyl diphosphates) as substrates. This resulted in 43 inhibitors with IC_{50} values in the 30 nM to 20 μ M range (Figure S1) when using GPP as substrate; 19 inhibitors with IC_{50} in the 600 nM to \sim 100 μ M range when using *cis*-FPP as substrate (Figure S2), and 53 inhibitors with IC_{50} as low as 650 nM using *trans*-FPP as a substrate.

We first carried out self-docking of the cocrystallized ligand CITPP into our *cis*-DPPS receptor grid center as a preliminary test of the ability to recover the crystallographic binding pose of the ligand. The docking pose shown in Figure S4 confirmed the validity of this grid center. We also investigated the possibility of the existence of other binding sites in DPPS using FTMap (50). The results of the FTMap analysis shown in Figure S5 suggest that DPPS does not have other binding sites. Therefore, we next proceeded to perform virtual screens (VSs) with the grid center located at the native binding site.

We evaluated VS receptor performance using the receiver operating characteristic (ROC) and area under the curve (AUC) metrics (47). AUC results using GPP as substrate are shown in Figures 8A and S6; for a *cis*-FPP substrate, in Figures 8B and S7; and for a *trans*-FPP substrate, in Figures 8C and S8. The populations of the apo DPPS MD structures (Figure 8) are in red and show that the most probable receptor volume is \sim 250 \AA^3 . In the case of GPP as substrate, the AUC results (Figure 8A, in blue; Figure S6) show that the top scoring receptors all have volumes \lesssim 300 \AA^3 . This cutoff is more pronounced when *cis*-FPP is used as the substrate (Figure 8B, in blue; Figure S7) where there is clearly a step-function behavior: Receptors with $V \gtrsim$ 300 \AA^3 have no predictive power in selecting actives from decoys, while 90% of receptors having $V >$ 300 \AA^3 have AUC $>$ 0.5 with the best receptors from the MD trajectory having AUC \sim 0.7, a considerable enrichment in actives. The reason for the presence of some enrichment at $V <$ 300 \AA^3 with GPP as substrate, while speculative, may be that the initial step in GPP chain elongation is being targeted by an inhibitor (which can bind to a smaller receptor pocket), while with *cis*-FPP as substrate, the normal chain elongation step is being targeted. In any case, with both systems, neither the most populated conformations nor any X-ray crystallographic receptors provided high predictive performance. The best performances with *cis*-FPP, the normal substrate, were observed with receptors 10, 22, and 30, with AUC values of 0.710, 0.726, and 0.662, corresponding active site volumes of 331 \AA^3 , 654 \AA^3 , and 882 \AA^3 , respectively (Figure S7).

With *trans*-FPP (Figures 8C and S8) as substrate, we found several of the smaller receptors performed well, a result that can be attributed to the larger number of small (bisphosphonate) inhibitors present in this subset of our screening library (compound structures are shown in Figure S3).

Overall, the ROC-AUC results clearly show that there are large enrichments of *cis*-DPPS actives possible using the MD-based structures, most of which are very rarely sampled, while the most frequently sampled conformations do not provide such enrichment as in many cases, the sizes of the inhibitors are larger than the most frequently sampled pocket volumes.

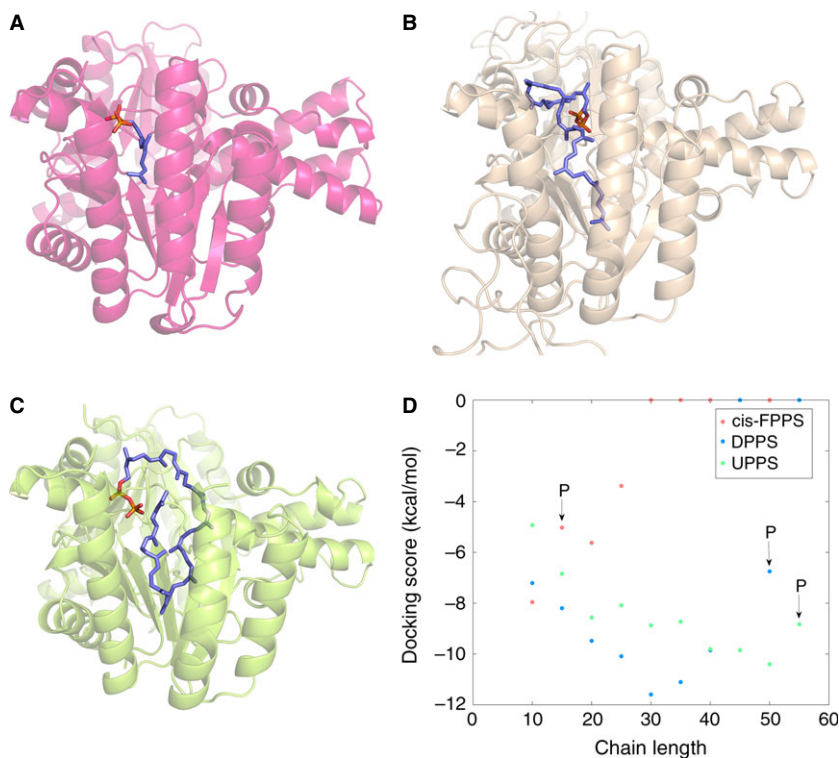


Figure 7: Docking poses of the products of the enzymes synthesizing prenyl molecules with various chain lengths. (A) *Cis*-FPPS + FPP. (B) *Cis*-DPPS + DPP. (C) UPPS + UPP. (D) Docking scores for the prenyl molecules with various chain lengths upon docking into *cis*-FPPS, *cis*-DPPS, and UPPS. The 'P' signs indicate the products of three enzymes.

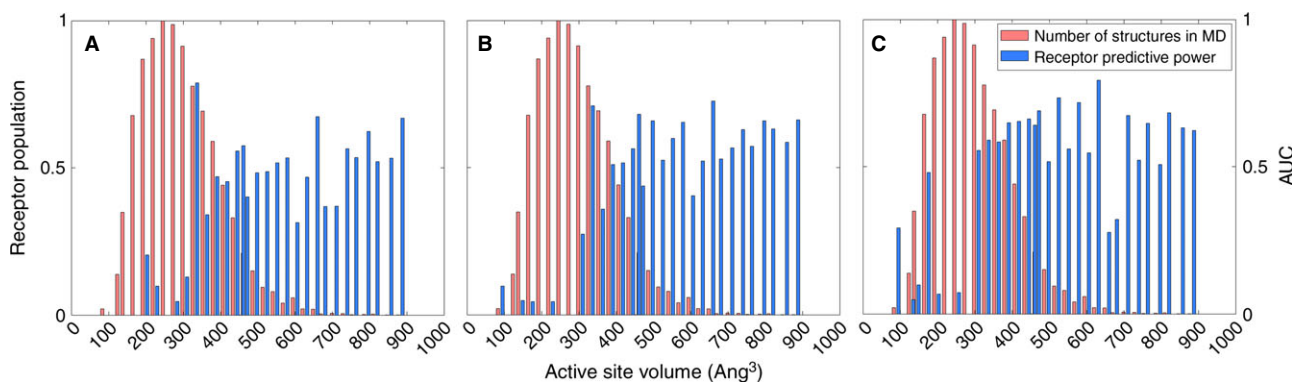


Figure 8: Correlation between the active site volume of the receptor and predictive performance in screening the compound library tested with: (A) GPP substrate; (B) *cis*-FPP substrate; (C) *trans*-FPP substrate.

Toward multitargeting of *cis*-FPPS, *cis*-DPPS, and Rv3378c

In previous work (11), we reported the X-ray crystallographic structure of Rv3378c in the presence of its substrate, tuberculosinyl diphosphate, as well as in the presence of an inhibitor, the bisphosphonate BPH-629 (Figure 1B). Bisphosphonates are often found to be good inhibitors of prenyl synthases as they contain a diphosphate group isostere, a bisphosphonate. For example, bisphosphonates are known potent inhibitors of UPPS as well as *trans*-FPPS (the latter inhibitors being used clinically to treat bone resorption diseases). However, there has been little progress in developing bisphosphonates that kill bacteria as they do not penetrate the bacterial cell wall. However, there are many other UPPS inhibitors

known, and many of the *cis*-DPPS inhibitors shown in Figure S1 also inhibit UPPS (7). We thus tested several of these (Figure S9) for activity against *cis*-FPPS and three (Figure S10) for activity against Rv3378c (using tuberculosinyl diphosphate and adenosine as substrates). The most potent inhibitor against Rv3378c was BPH-629, which had an IC_{50} of 210 nM (and an IC_{50} of 610 nM against DPPS, using *cis*-FPP as substrate). However, BPH-629 was inactive against the *M. tuberculosis* model, *M. smegmatis*. In contrast, the bisamidine BPH-1417 (Figure 1B) had an IC_{50} = 0.5–20 μ M, depending on substrate against DPPS as well as an IC_{50} = 660 nM against Rv3378c. In addition, it also inhibited *cis*-FPPS (Figure S9) with an IC_{50} of 4.8 μ M. Glide docking poses to all three enzymes are shown in Figure 9 and show

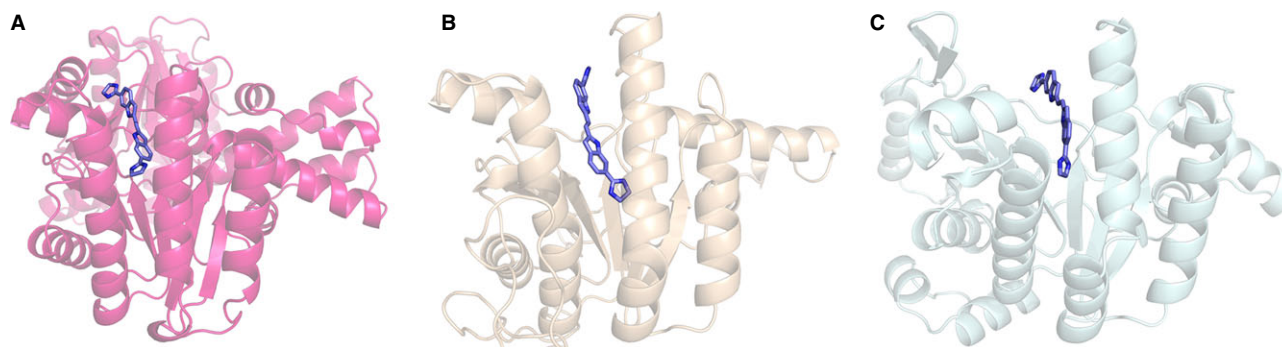


Figure 9: Predicted docking poses for BPH-1417. (A) *Cis*-FPPS. (B) *Cis*-DPPS. (C) Rv3378c.

that in each case, the substrate site, that is, site 1, is likely to be occupied.

In previous work (7), we showed that the bisamidine BPH-1358 (Figure S11) was a potent UPPS inhibitor that also had *in vivo* activity in a *S. aureus* mouse model of infection (7), but BPH-1358 was inactive here against Rv3378c. However, the bisamidine BPH-1417 has potent *in vitro* as well as *in vivo* activity against *S. aureus* and has also been reported to have an MIC in the 0.3–1.3 $\mu\text{g}/\text{mL}$ range against *M. tuberculosis* (51). It is likely that DNA is also a target in these organisms (as with other bisamidines), and the ability to potentially target DNA, cell wall biosynthesis (*cis*-FPPS/*cis*-DPPS), and virulence factor formation (Rv3378c) is clearly of interest in the context of multitarget inhibitor development (52) for drug-resistant infections.

Conclusions

In this work, we carried out MD simulations of three prenyl synthase enzymes from *M. tuberculosis*: *cis*-FPPS (Rv1086c); *cis*-DPPS (Rv2361c); and tuberculosinol/tuberculosinyl adenosine synthase (Rv3378c), proteins which all contain a ζ -fold structure with *cis*-DPPS and Rv3378c being of interest as new tuberculosis drug targets. *Cis*-DPPS exhibited large active site pocket volume fluctuations in its apo and IPP-bound forms, but not in the presence of the substrate-like inhibitor, CITPP. The largest volume was $V = 882 \text{ \AA}^3$, very close to that of the *cis*-DPP product ($V = 879 \text{ \AA}^3$). With *cis*-FPPS, the volumes were as expected much smaller but increased to up to $\sim 537 \text{ \AA}^3$ in the MD simulation. For UPPS, the largest pocket volume in MD is 1032 \AA^3 , close to the volume of UPP ($V \sim 965 \text{ \AA}^3$). We used the FPPS, DPPS, and UPPS MD structures to examine the chain length dependence of ligand binding energies using C_{10} – C_{60} prenyl diphosphates, to help elucidate chain length regulation mechanisms. The most favorable binding energies were found with compounds having chain lengths shorter than the products, where energies were $\approx 3 \text{ kcal/mol}$ higher than the lowest energies seen. Chains that were ~ 2 prenyls longer than products either did not dock or had

very poor docking scores. We then used a PCA method to analyze the X-ray structures of *cis*-FPPS, *cis*-DPPS, and UPPS, together with results from *cis*-FPPS and *cis*-DPPS MD trajectories. The FPPS/DPPS structures clustered most closely with closed (substrate-like liganded) UPPS structures, presumably because many (open or ajar) UPPS structures have multiple bound ligands, while *cis*-FPPS and *cis*-DPPS do not. That is, the UPPS structures do not necessarily mimic normal product-bound structures (as evidenced also by their pocket volumes which in many cases are considerably larger than the UPP product volume). Finally, we investigated the inhibition of *cis*-DPPS by a range of putative prenyl transferase inhibitors, finding several potent leads. Using these results, we found using the ROC-AUC method that MD-based structures with receptor volumes $>300 \text{ \AA}^3$, in general, gave the best ROC-AUC values (~ 0.7). We also tested several of the *cis*-DPPS inhibitors for activity against *cis*-FPPS and Rv3378c. Bisphosphonates and bisamidines had activity against several targets, the best being BPH-1417 which was a 660-nM inhibitor of Rv3378c, a 4.8- μM inhibitor of *cis*-FPPS, and a 1.3- μM inhibitor of *cis*-DPPS, results that open up the possibility of multitarget inhibition in which both cell wall biosynthesis and virulence factor formation may be inhibited.

Acknowledgments

This work was supported by the National Science Foundation, the United States Public Health Service (NIH grants CA158191, GM031749, and GM065307); the Howard Hughes Medical Institute; the National Biomedical Computation Resource; the UCSD Center for Theoretical Biological Physics; a Harriet A. Harlin Professorship (E.O.); the University of Illinois Foundation/Oldfield Research Fund; and a Molecular Biophysics Training Grant from the NIH. F. F. acknowledges financial support of the Beatriu de Pinós program from AGAUR for a postdoctoral grant (2010 BP_A 00339). X.F. was supported by an American Heart Association, Midwest Affiliate, Pre-Doctoral Fellowship (13PRE14510056).

References

1. Chambers H.F., DeLeo F.R. (2009) Waves of resistance: *Staphylococcus aureus* in the antibiotic era. *Nature Rev Microbiol*;7:629–641.
2. Fischbach M.A., Walsh C.T. (2009) Antibiotics for emerging pathogens. *Science*;325:1089–1093.
3. Antibiotic Resistance Threats in the United States. (2013) US Department of Health and Human Services Centers for Disease Control and Prevention.
4. Antimicrobial resistance: global report on surveillance 2014. World Health Organization.
5. Peukert S., Sun Y., Zhang R., Hurley B., Sabio M., Shen X., Gray C., Dzink-Fox J., Tao J., Cebula R. (2008) Design and structure-activity relationships of potent and selective inhibitors of undecaprenyl pyrophosphate synthase (UPPS): tetramic, tetrionic acids and dihydropyridin-2-ones. *Bioorg Med Chem Lett*;18:1840–1844.
6. Guo R.-T., Cao R., Liang P.-H., Ko T.-P., Chang T.-H., Hudock M.P., Jeng W.-Y., Chen C.K.-M., Zhang Y., Song Y. (2007) Bisphosphonates target multiple sites in both cis- and trans-prenyltransferases. *Proc Natl Acad Sci USA*;104:10022–10027.
7. Zhu W., Zhang Y., Sinko W., Hensler M.E., Olson J., Molohon K.J., Lindert S. *et al.* (2013) Antibacterial drug leads targeting isoprenoid biosynthesis. *Proc Natl Acad Sci USA*;110:123–128.
8. Jeong Y.C., Anwar M., Bikadi Z., Hazai E., Moloney M.G. (2013) Natural product inspired antibacterial tetramic acid libraries with dual enzyme inhibition. *Chem Sci*;4:1008–1015.
9. Sassetti C.M., Boyd D.H., Rubin E.J. (2003) Genes required for mycobacterial growth defined by high density mutagenesis. *Mol Microbiol*;48:77–84.
10. Oldfield E., Lin F.Y. (2012) Terpene biosynthesis: modularity rules. *Angew Chem Int Ed*;51:1124–1137.
11. Chan H.-C., Feng X., Ko T.-P., Huang C.-H., Hu Y., Zheng Y., Bogue S. *et al.* (2014) Structure and inhibition of tuberculosin synthase and decaprenyl diphosphate synthase from *Mycobacterium tuberculosis*. *J Am Chem Soc*;136:2892–2896.
12. Layre E., Lee H.J., Young D.C., Martinot A.J., Buter J., Minnaard A.J., Annand J.W., Fortune S.M., Snider B.B., Matsunaga I., Rubin E.J., Alber T., Moody D.B. (2014) Molecular profiling of *Mycobacterium tuberculosis* identifies tuberculosinyl nucleoside products of the virulence-associated enzyme Rv3378c. *Proc Natl Acad Sci USA*;111:2978–2983.
13. Hoshino T., Nakano C., Ootsuka T., Shinohara Y., Hara T. (2011) Substrate specificity of Rv3378c, an enzyme from *Mycobacterium tuberculosis*, and the inhibitory activity of the bicyclic diterpenoids against macrophage phagocytosis. *Org Biomol Chem*;9:2156–2165.
14. Mann F.M., Xu M.M., Chen X.M., Fulton D.B., Russell D.G., Peters R.J. (2009) Edaxadiene: a new bioactive diterpene from *Mycobacterium tuberculosis*. *J Am Chem Soc*;131:17526–17527.
15. Prach L., Kirby J., Keasling J.D., Alber T. (2010) Diterpene production in *Mycobacterium tuberculosis*. *FEBS J*;277:3588–3595.
16. Pethe K., Swenson D.L., Alonso S., Anderson J., Wang C., Russell D.G. (2004) Isolation of *Mycobacterium tuberculosis* mutants defective in the arrest of phagosome maturation. *Proc Natl Acad Sci USA*;101:13642–13647.
17. Wang W., Dong C., McNeil M., Kaur D., Mahapatra S., Crick D.C., Naismith J.H. (2008) The structural basis of chain length control in Rv1086. *J Mol Biol*;381:129–140.
18. Durrant J.D., Cao R., Gorfe A.A., Zhu W., Li J., Sankovsky A., Oldfield E., McCammon J.A. (2011) Non-bisphosphonate inhibitors of isoprenoid biosynthesis identified via computer-aided drug design. *Chem Biol Drug Des*;78:323–332.
19. Case D.A., Cheatham T.E. III, Darden T., Gohlke H., Luo R., Merz K.M. Jr, Onufriev A., Simmerling C., Wang B., Woods R.J. (2005) The Amber biomolecular simulation programs. *J Comput Chem*;26:1668–1688.
20. Jorgensen W.L., Chandrasekhar J., Madura J.D., Impey R.W., Klein M.L. (1983) Comparison of simple potential functions for simulating liquid water. *J Chem Phys*;79:926–935.
21. Case D.A., Darden T.A., Cheatham T.E. III, Simmerling C.L., Wang J., Duke R.E., Luo R. *et al.* (2010) AMBER 11. San Francisco: University of California.
22. Hornak V., Abel R., Okur A., Strockbine B., Roitberg A., Simmerling C. (2006) Comparison of multiple Amber force fields and development of improved protein backbone parameters. *Proteins*;65:712–725.
23. Lindorff-Larsen K., Piana S., Palmo K., Maragakis P., Klepeis J.L., Dror R.O., Shaw D.E. (2010) Improved side-chain torsion potentials for the Amber ff99SB protein force field. *Proteins*;78:1950–1958.
24. Ryckaert J.-P., Ciccotti G., Berendsen H.J.C. (1977) Numerical integration of the cartesian equations of motion of a system with constraints: molecular dynamics of n-alkanes. *J Comput Phys*;23:327–341.
25. Schulbach M.C., Mahapatra S., Macchia M., Barontini S., Papi C., Minutolo F., Bertini S., Brennan P.J., Crick D.C. (2001) Purification, enzymatic characterization, and inhibition of the Z-farnesyl diphosphate synthase from *Mycobacterium tuberculosis*. *J Biol Chem*;276:11624–11630.
26. Li H., Robertson A.D., Jensen J.H. (2005) Very fast empirical prediction and interpretation of protein pKa values. *Proteins*;61:704–721.
27. Bas D.C., Rogers D.M., Jensen J.H. (2008) Very fast prediction and rationalization of pKa values for protein-ligand complexes. *Proteins*;73:765–783.
28. Olsson M.H.M., Søndergaard C.R., Rostkowski M., Jensen J.H. (2011) PROPKA 3: consistent treatment of internal and surface residues in empirical pKa predictions. *J Chem Theory Comput*;7:525–537.
29. Søndergaard C.R., Olsson M.H.M., Rostkowski M., Jensen J.H. (2011) Improved treatment of ligands and

- coupling effects in empirical calculation and rationalization of pKa values. *J Chem Theory Comput*;7:2284–2295.
30. Gordon J.C., Myers J.B., Folta T., Shoja V., Heath L.S., Onufriev A. (2005) H++: a server for estimating pKas and adding missing hydrogens to macromolecules. *Nucleic Acids Res*;33:W368–W371.
 31. Myers J., Grothaus G., Narayanan S., Onufriev A. (2006) A simple clustering algorithm can be accurate enough for use in calculation of pKs in macromolecules. *Proteins*;63:928–938.
 32. Anandakrishnan R., Aguilar B., Onufriev A.V. (2012) H++ 3.0: automating pK prediction and the preparation of biomolecular structures for atomistic molecular modeling and simulation. *Nucleic Acids Res*;40:537–541.
 33. H++: Web-based computational prediction of protonation states and pK of ionizable groups in macromolecules.
 34. Frisch M.J., Trucks G.W., Schlegel H.B., Scuseria G.E., Robb M.A., Cheeseman J.R., Montgomery J.A. Jr *et al.* (2004) Gaussian 03. Wallingford, CT: Gaussian Inc.
 35. Wang J., Wolf R.M., Caldwell J.W., Kollman P.A., Case D.A. (2004) Development and testing of a general AMBER force field. *J Comput Chem*;25:1157–1174.
 36. Wang J., Wang W., Kollman P.A., Case D.A. (2006) Automatic atom type and bond type perception in molecular mechanical calculations. *J Mol Graphics Modell*;25:247–260.
 37. Durrant J.D., de Oliveira C.A.F., McCammon J.A. (2011) POVME: an algorithm for measuring binding-pocket volumes. *J Mol Graphics Modell*;29:773–776.
 38. Grant B.J., Rodrigues A.P.C., ElSawy K.M., McCammon J.A., Caves L.S.D. (2006) Bio3D: an R package for the comparative analysis of protein structures. *Bioinformatics*;22:2695–2696.
 39. Shelley J.C., Cholleti A., Frye L., Greenwood J.R., Timlin M.R., Uchimaya M. (2007) Epik: a software program for pKa prediction and protonation state generation for drug-like molecules. *J Comput Aided Mol Des*;21:681–691.
 40. Greenwood J.R., Calkins D., Sullivan A.P., Shelley J.C. (2010) Towards the comprehensive, rapid, and accurate prediction of the favorable tautomeric states of drug-like molecules in aqueous solution. *J Comput Aided Mol Des*;24:591–604.
 41. Friesner R.A., Banks J.L., Murphy R.B., Halgren T.A., Klicic J.J., Mainz D.T., Repasky M.P., Knoll E.H., Shaw D.E., Shelley M., Perry J.K., Francis P., Shenkin P.S. (2004) Glide: a new approach for rapid, accurate docking and scoring. 1. Method and assessment of docking accuracy. *J Med Chem*;47:1739–1749.
 42. Halgren T.A., Murphy R.B., Friesner R.A., Beard H.S., Frye L.L., Pollard W.T., Banks J.L. (2004) Glide: a new approach for rapid, accurate docking and scoring. 2. Enrichment factors in database screening. *J Med Chem*;47:1750–1759.
 43. Friesner R.A., Murphy R.B., Repasky M.P., Frye L.L., Greenwood J.R., Halgren T.A., Sanschagrin P.C., Mainz D.T. (2006) Extra Precision Glide: docking and scoring incorporating a model of hydrophobic enclosure for protein-ligand complexes. *J Med Chem*;49:6177–6196.
 44. Webb M.R. (1992) A continuous spectrophotometric assay for inorganic phosphate and for measuring phosphate release kinetics in biological systems. *Proc Natl Acad Sci USA*;89:4884–4887.
 45. Amaro R.E., Baron R., McCammon J.A. (2008) An improved relaxed complex scheme for receptor flexibility in computer-aided drug design. *J Comput Aided Mol Des*;22:693–705.
 46. Brenke R., Kozakov D., Chuang G.-Y., Beglov D., Hall D., Landon M.R., Mattos C., Vajda S. (2009) Fragment-based identification of druggable ‘hot spots’ of proteins using Fourier domain correlation techniques. *Bioinformatics*;25:621–627.
 47. Fawcett T. (2006) An introduction to ROC analysis. *Pattern Recognit Lett*;27:861–874.
 48. Teng K.H., Liang P.H. (2012) Structures, mechanisms and inhibitors of undecaprenyl diphosphate synthase: a cis-prenyltransferase for bacterial peptidoglycan biosynthesis. *Bioorg Chem*;43:51–57.
 49. Wallrapp F.H., Pan J.-J., Ramamoorthy G., Almonacid D.E., Hillerich B.S., Seidel R., Patskovsky Y., Babbitt P.C., Almo S.C., Jacobson M.P. (2013) Prediction of function for the polyprenyl transferase subgroup in the isoprenoid synthase superfamily. *Proc Natl Acad Sci USA*;110:1196–1202.
 50. Ngan C.H., Bohnuud T., Mottarella S.E., Beglov D., Villar E.A., Hall D.R., Kozakov D., Vajda S. (2012) FTMAP: extended protein mapping with user-selected probe molecules. *Nucleic Acids Res*;40:W271–W275.
 51. Panchal R.G., Lane D., Boshoff H.I., Butler M.M., Moir D.T., Bowlin T.L., Bavari S. (2013) Bis-imidazolinyldoles are active against methicillin-resistant *Staphylococcus aureus* and multidrug-resistant *Mycobacterium tuberculosis*. *J Antibiot*;66:47–49.
 52. Morphy R., Harris J. (2012) Designing multi-target drugs preface. *R Soc Chem*; Xv–Xvii.

Notes

^a(2012) Maestro, version 9.3. New York, NY: Schrödinger, LLC.

^b(2012) LigPrep, version 2.5. New York, NY: Schrödinger, LLC.

^c(2012) Epik, version 2.3. New York, NY: Schrödinger, LLC.

^q(2012) Glide, version 5.8. New York, NY: Schrödinger, LLC.



Supporting Information

Additional Supporting Information may be found in the online version of this article:

Figure S1. Structures and IC_{50} values (in μM) for *cis*-DPPS inhibitors in a GPP-based assay.

Figure S2. Structures and IC_{50} values (in μM) for *cis*-DPPS inhibitors in a *cis*-FPP-based assay.

Figure S3. Structures and IC_{50} values (in μM) for *cis*-DPPS inhibitors in a *trans*-FPP-based assay.

Figure S4. Comparison of the docking pose of the co-crystallized ligand CITPP self-docked into the receptor grid center with its crystallographic orientation in the 2VG3 crystal structure.

Figure S5. Potential ligand binding sites of DPPS predicted by FTMap.

Figure S6. ROC-AUC results for *cis*-DPPS inhibition (GPP substrate) using X-ray and MD structures.

Figure S7. ROC-AUC results for *cis*-DPPS inhibition (*cis*-FPP substrate) using X-ray and MD structures.

Figure S8. ROC-AUC results for *cis*-DPPS inhibition (*trans*-FPP substrate) using X-ray and MD structures.

Figure S9. Structures and IC_{50} values (in μM) for *cis*-FPPS inhibitors.

Figure S10. Structures and IC_{50} values (in μM) for Rv3378c inhibitors.

Table S1. Pocket volumes of various structures of *cis*-FPPS, DPPS, and UPPS and their corresponding conformational states.